1998

Inversion of Plasmaspheric EUV Remote Sensing Data from the STP 72-1 Satellite

R.R. Meier
Naval Research laboratory

A.C. Nicholas
Praxis, Inc.

J.M. Picone
Naval Research laboratory

D.J. Melendez-Alvira
Naval Research laboratory

G. Ganguli
Naval Research laboratory

See next page for additional authors

JOURNAL OF GEOPHYSICAL RESEARCH, VOL. 103, NO. A8, PAGES 17,505–17,518, AUGUST 1, 1998

Inversion of plasmaspheric EUV remote sensing data from the STP 72-1 satellite

R. R. Meier,[1] A. C. Nicholas,[2] J. M. Picone,[1] D. J. Melendez-Alvira,[1] G. I. Ganguli,[3] M. A. Reynolds,[3] and E. C. Roelof[4]

Abstract. Observations of the extreme ultraviolet emission of helium ions at 30.4 nm can be used to study the global shape of the plasmasphere and its dynamical response to geomagnetic forcing. In order to retrieve number densities of plasmaspheric He^+ from such observations, we have developed a new inversion technique based on discrete inverse theory, which uses the optical data to optimize a parameterized model of the He^+ distribution. We apply this inversion technique to several orbits of data obtained from the Naval Research Laboratory extreme ultraviolet photometric experiment launched on the STP 72-1 satellite in October 1972. The inversion is limited to nighttime conditions where contamination from the topside ionosphere is minimal and where a simple parameterization of the He^+ number density is applicable. We obtain excellent fits to the data; however, some of the retrieved model parameters have large uncertainties due to inadequate sampling of the plasmasphere. Our study shows that improved sampling using observations from different locations and view directions would significantly enhance the accuracy of the retrieved model parameters. Using a newly developed three-dimensional imaging tool to visualize the plasmaspheric regions being sampled remotely, we demonstrate that emission features observed from two of the STP 72-1 orbits originate beyond the plasmasphere. Estimated number densities of this feature are roughly consistent with observations of cold plasma seen at geosynchronous orbit by in situ experiments.

1. Introduction

Photometric experiments carried out for more than 25 years have shown that the plasmasphere can be sensed remotely through the measurement of the extreme ultraviolet (EUV) emission line of helium ions at 30.4 nm. Both rocket [*Johnson et al.*, 1971; *Meier and Weller*, 1972; *Paresce et al.*, 1974; *Yoshikawa et al.*, 1997] and satellite [*Weller and Meier*, 1974; *Chakrabarti et al.*, 1982; also see *Jelinsky et al.*, 1995] missions have demonstrated agreement of the optical data with models of resonant scattering of the solar emission line by plasmaspheric He^+. All of the plasmaspheric remote sensing data obtained so far have been from low Earth orbit (LEO), providing "inside-out" views.

With the surge of interest in global imaging of the magnetosphere [e.g., see *Williams et al.*, 1992, and references therein], EUV remote sensing of the plasmasphere has become one of the three prime methods of achieving that capability, the other two being energetic neutral atom and auroral imaging. A NASA Magnetospheric Imager Mission concept definition [*Armstrong and Johnson*, 1995] was followed by the selection of the Imager for Magnetopause-to-Aurora Global Exploration (IMAGE) as a Medium-Class Explorer (MIDEX) mission (see the web site http://image.gsfc.nasa.gov for more information). This mission will reach 8 E_R apogee to achieve global mapping of the inner magnetosphere. Another imager, the extreme ultraviolet imaging photometer, is planned for flight in LEO aboard the STP (U.S. Air Force Space Test Program) ARGOS satellite to be launched within the next year (see the web site http://www.te.plk.af.mil/arpics/apage4.htm). There are also plans for an imaging mission from a lunar vantage point [*Yoshikawa et al.*, 1997].

Lacking so far in the plasmaspheric imaging concept is a quantitative measure of the information about the number density of helium ions (a three-dimensional quantity) which is retrievable from remote sensing images (essentially two-dimensional in character). All of the analyses published so far have used the forward modeling approach in which predictions are made of the emission rate, compared with data, and the model parameters are adjusted until the agreement is deemed acceptable. Herein we develop a formalism for inverting plasmaspheric remote sensing data based on the principles of discrete inverse theory (DIT) [see *Tarantola and Valette*, 1982; *Tarantola*, 1987; *Menke*, 1989; *Picone et al.*, 1997a].

The objective of this work is to demonstrate how well plasmaspheric parameters can be retrieved from EUV remote sensing data. In this initial phase of the work we have limited the approach to photometric observations (i.e., narrow scans in specific directions), leaving the application to full images for the future. Data from the Naval Research Laboratory (NRL) EUV experiment on the STP 72-1 satellite [*Weller and Meier*, 1974] provide an excellent opportunity to test the retrieval method for LEO observing platforms. Consequently, we have resurrected a limited set of data from that mission. However,

[1]E. O. Hulburt Center for Space Research, Naval Research Laboratory, Washington, D. C.
[2]Praxis, Inc., Alexandria, Virginia.
[3]Plasma Physics Division, Naval Research Laboratory, Washington, D. C.
[4]Applied Physics Laboratory, Johns Hopkins University, Laurel, Maryland.

Paper number 98JA01175.
0148-0227/98/98JA-01175$09.00

Table 1. STP 72-1 Mission and NRL EUV Instrument

Flight Parameters	Geophysical Conditions	Instrumentation
Launch, October 2, 1972	F_{10} = 90 – 120	five Photometers, 17–150 nm total passband
Orbit, 740 km altitude	Ap = 3–34 for orbits analyzed	detectors, spiral channeltron
Inclination, 98.3°		ND5, Al/C filter (17–60 nm passband)
Local time, noon/midnight		ND4, Al filter (17–80 nm passband)
Orientation, spinning at 5 s period		ND1, indium (75–105 nm passband)
		fields-of-view, 9° full width at half maximum
		orientation, 25° from orbital plane (115° from spin vector)

since Weller and Meier were unable to fit the nighttime observations with a simple parameterized model of the plasmasphere, the first task in this project was to determine if the data could be reproduced at all. The next task was to invert the observations to obtain the optimal set of parameters and to use the DIT diagnostics to establish the quality of the retrieved parameters. Last, we considered ways to improve the remote sensing approach from LEO, especially using (synthetic) data from more than a single observing site.

We begin the paper with a review of the STP 72-1 mission and data and the optical model and the plasmasphere parameterization, and then we develop the DIT application to plasmaspheric remote sensing. The remainder of the paper follows the tasks described above, including a description of a new system for visualizing and interpreting the complicated geometric features seen in EUV remote sensing data.

2. STP 72-1 Mission and EUV Data

The STP 72-1 satellite was placed into Earth orbit on October 2, 1972. The NRL EUV instrument began operations 3 days later. Details are given by *Weller and Meier* [1974] and *Meier and Weller* [1974]. Briefly, the orbit is approximately circular at about 740 km altitude and 98.3° inclination. This configuration kept the Sun-Earth vector in the orbital plane, a noon–midnight orbit. The spin axis of the satellite was maintained normal to the orbital plane in a so-called "cartwheel" configuration. The NRL instrument line of sight (LOS) was canted 25° from the spin (and orbital) plane to avoid viewing the Sun during the day. In one rotation of the spacecraft the instrument viewed within 25° of the local vertical, swept to the horizon, then to within 25° of nadir, across the alternate horizon, and back up to near zenith. The instrument pointed toward earlier local times during the day and later local times at night. A brief summary of flight and instrument information is given in Table 1. A sketch of the orbital geometry is given in Figure 2 of *Weller and Meier* [1974].

The NRL payload contained five photometers spanning the wavelength band 17–150 nm, three of which covered the EUV spectral region below 100 nm. These three bands are listed in Table 1. Light entering a photometer was confined to a 9° full field of view (FOV) by a collimator and baffles. Light then passed through a filter wheel and was detected by spiral channeltrons. Photometers ND4 and ND5 were sensitive to both He I 58.4 nm and He II 30.4 nm radiation. The responsivity of ND4 was 40.0 counts s^{-1} R^{-1} at 30.4 nm and 13.8 counts s^{-1} R^{-1} at 58.4 nm. The responsivity of ND5 was 42.5 counts s^{-1} R^{-1} at 30.4 nm and 0.41 counts s^{-1} R^{-1} at 58.4 nm. ND5 was the primary sensor for detecting He II 30.4 nm emission. When both 58.4 and 30.4 nm emissions were present, the responses of both photometers were combined to derive the individual emission rates.

The data set obtained from this mission was sparse. Typical instrument operations were limited to two nighttime orbital passes every other day and a full pass every 2 weeks. In actuality, even fewer passes were obtained over the approximately 18 months of instrument operations. Only data taken at the closest approach of the LOS to zenith and nadir have been archived and are still available for analysis. Unfortunately, the only archive medium remaining is paper strip charts, which include the data and the attitude-orbit information. As will be seen later, the missing spin-scan data would have been quite valuable for improving the retrieval of model parameters. Twenty of the orbital passes viewing near zenith have been digitized, courtesy of G. R. Gladstone, and are now available for analysis. We have chosen six representative passes for detailed analysis.

An example of the near-zenith emission rate of plasmaspheric He^+ is shown for orbit 650 in Figure 3 of *Weller and Meier* [1974]. Examples from orbit 650 and three additional orbits are shown in Figure 1 in a somewhat different format. In each plot Earth is at the center of the plot, with lines of geomagnetic latitude and longitude superimposed. The smooth solid lines display the L = 4 dipole lines of the magnetic field, which approximate the boundary of open and closed field lines (the plasmapause). Magnetic north is vertically upward. The antisolar direction is indicated with arrows to the left of each orbit depiction, and the Earth shadow is shown by the shaded regions to the right. The satellite altitude of 740 km is approximated by the innermost dotted circle. The FOV of the EUV experiment is indicated in the top left. The 25° cant out of the orbital plane is behind the plane of Figure 1. As the satellite progresses around in orbit, the emission rates are plotted radially outward as points connected with a thin irregular line. The zero emission rate level coincides with the orbital location, and the 3 and 6 R levels are also shown as dotted circles. While the satellite orbit was usually not positioned along a magnetic meridian (although the solar vector was in the orbital plane) and the projections into the Figure 1 plane are not exact, this form of data display provides a useful framework for visualizing the observations from low Earth orbit. For example, if the plasmasphere and topside ionosphere were (albeit unrealistically) uniformly filled with helium ions, the emission rate curve would track the dipole field lines during the day.

The emission rate shows large decreases over the polar regions, consistent with the lack of high-latitude helium ions on open field lines. The emission rate is fairly smooth during the day but structured at night in part because of the Earth shadow cutting through the plasmasphere. The examples shown in

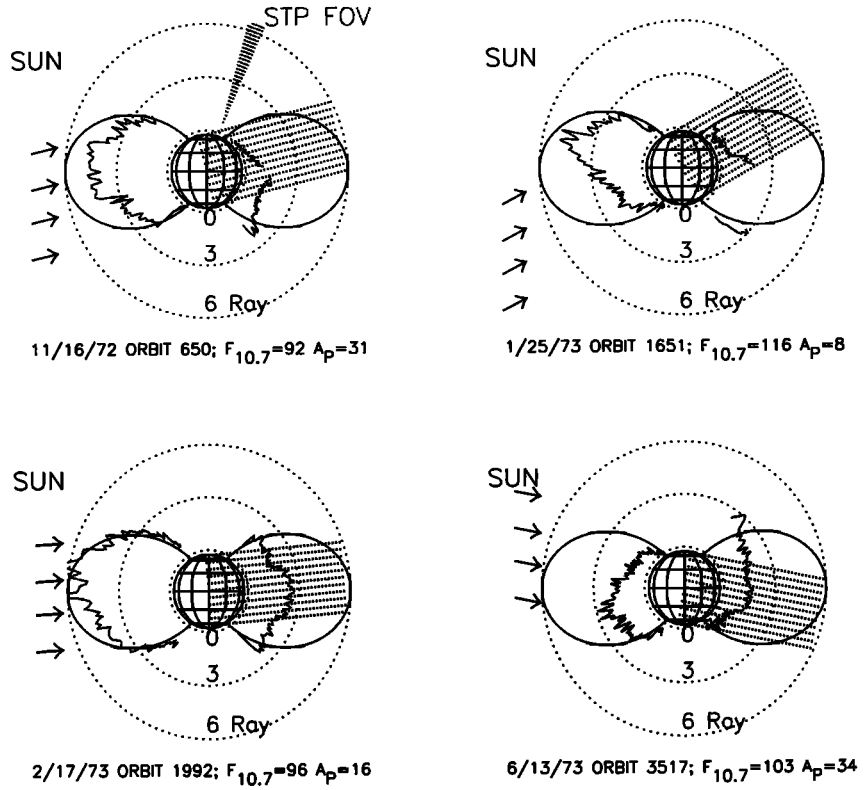

Figure 1. Equatorial display of STP 72-1 He II 30.4 nm column emission rates. Geomagnetic latitude and longitude are drawn on the Earth at the center. $L = 4$ dipole lines are shown. Arrows indicate the antisolar direction; the shadow is shown by the shaded region. The field of view (FOV) of the EUV experiment is shown in the top left. The 25° cant out of the orbital plane is behind the plane of Figure 1. The innermost dotted circle indicates the satellite altitude. Column emission rates are plotted radially outward from the satellite position. The zero emission rate level coincides with the orbital location, and the 3 and 6 R levels are also shown as dotted circles. See text.

Figure 1 display the diversity of structure seen in the data. The point-to-point variations are due to counting statistics. A few data gaps can be seen in the individual orbit depictions. Comparison of the plasmaspheric emission morphology with that of the tropical arcs [*Anderson et al.*, 1976] clearly demonstrates that there is no ionospheric O^+ airglow contamination of the signal from ND4 or ND5 photometers.

As will be discussed in section 5.4, the daytime observations from LEO contain substantial foreground emission from the topside ionosphere; consequently, we will concentrate on the analysis of nighttime observations in this work. At night most of the emission comes from the plasmasphere since the ionosphere is usually shadowed. As well, much better diagnostic information is available at night because of the action of the Earth shadow as a height differentiator of the emission rate. We will show in section 5.3 that this is particularly compelling where measurements in the shadow direction reveal plasma from beyond the plasmasphere.

Early attempts at modeling the STP 72-1 data were fortuitously successful during the day (see above) but failed to reproduce the emission rate during the night [*Weller and Meier*, 1974]. A reexamination of the raw data has revealed the main source of the difficulty. The latitudinal range of disagreement between models and data turns out to be closely associated with EUV equatorial bands seen in the nadir by both photometers ND4 and ND5 [*Meier and Weller*, 1975]. No emission was seen in photometer ND1. The emission rate reported by those authors has morphological characteristics in common with low-altitude quasi-trapped high-energy helium ions [*Scholer et al.*, 1975]. *Meier and Weller* [1975] attributed the emission rate to the recombination/electron capture spectrum of He^{++} into He^+ taking place well below the 740 km spacecraft orbit (~150 km). The spin-scan data revealed strong support for a low-altitude origin of the signal [*Meier and Weller*, 1975, Figure 5]. During the present reexamination we discovered that there is also an effect of these bands in the data taken in the near-zenith direction. Careful scrutiny of the raw data shows a slight rise in signal correlated with the occurrence of EUV bands in the nadir. This rise is masked to a large extent because it compensates for the drop in He II 30.4 nm plasmaspheric emission when viewing toward Earth's shadow. Observations by other experiments [*Chakrabarti et al.*, 1982] show little or no emission when viewing directly down the shadow. *Paresce et al.* [1983] suggest that as much as 0.02 R is possible in the data of Chakrabarti et al. A weak sub-Rayleigh emission from the shadow region was detected from Extreme Ultraviolet Explorer [*Jelinsky et al.*, 1995], which may be due to a small amount of secondary scattering [*Meier and Weller*, 1972, equation (18)], even though the plasmasphere is optically thin for practical purposes.

This contamination of the near-zenith data is puzzling. There is too little atmosphere above 740 km to allow for recombination radiation or charge capture by energetic helium ions. Perhaps a small part of the apparent emission from the

nadir is actually due to energetic particles passing through the thin metal film filters and impacting the detector. This would be present in the zenith as well and could account for the signal recorded by ND4 and ND5 and for the lack of detection by ND1, since its filter is made of indium with atomic mass much greater than aluminum. In any case, data near the magnetic dip equator were excluded from the present analysis by using the much stronger nadir-viewing detections of the EUV bands to identify the regions of contamination in the near-zenith data.

3. Forward Model

The "forward model" is a description of resonant scattering of solar 30.4 nm emission line photons by helium ions in the terrestrial plasmasphere. It is used to predict the results of optical measurements based on the observing geometry, the resonant scattering process, and a parameterized model of the plasmaspheric He^+ number density distribution. Conventional forward analysis consists of adjusting the parameters of the model until a fit is obtained to data which is judged adequate by some (hopefully) objective criteria. An alternative approach, which we introduce in section 4, is to use discrete inverse theory to retrieve model parameters from the remote sensing data. The forward model forms the core of our inversion procedure, which systematically adjusts the parameters characterizing the He^+ number density distribution to obtain an optimal fit of model intensity values to the measurements. The resulting model parameter values then define the maximum likelihood He^+ distribution underlying the observations. In this section we describe the forward optical model, which contains the geometry and the scattering process, and the parameterized model of the ion distribution.

3.1. Optical Model

The original optical model was presented by *Meier and Weller* [1972] and has not changed except for the parameterization of the He^+ concentration. It is useful to review here the relationships between the observed column emission rate and the ion number density to set the stage for the inverse problem.

The plasmasphere is optically thin at 30.4 nm [*Meier and Weller*, 1972]; thus the column emission rate, $4\pi I$ (Rayleigh), can be written as

$$4\pi \mathrm{I} = g\phi(\theta) N_{\mathrm{He}}/10^6, \tag{1}$$

where g is the scattering rate of solar photons, ϕ is the phase function for scattering through angle θ, and N_{He} is the column number density of helium ions. The g factor (photon s^{-1} ion^{-1}) is defined as

$$g = \int F_{\mathrm{Sun}}(\lambda)\sigma(\lambda)\, d\lambda = \frac{\pi e^2}{mc} f_{12} F_{\mathrm{Sun}}(\upsilon_0), \tag{2}$$

where F_{Sun} is the solar 30.4 nm photon flux (photon cm^{-2} s^{-1} nm^{-1}) and σ is the resonant scattering cross section at wavelength λ. In (2), f_{12} is the transition oscillator strength, and the other factors are the usual fundamental constants. Since the solar emission line is much broader than the plasmaspheric line width, the solar flux can be taken out of the integral. Converting the solar flux at line center, $\lambda_0 = 30.387$ nm, into units of photon cm^{-2} s^{-1} Hz^{-1} ($F_{\mathrm{Sun}}(\upsilon_0)$, where υ_0 is the line center frequency), and using the standard form for the cross section, the right-hand side of the equation results [*Meier*, 1991].

He^+ has the same electronic configuration as atomic hydrogen. Since helium has zero nuclear magnetic moment, the phase function should also be the same as for hydrogen but without hyperfine splitting. In deriving the phase function for atomic hydrogen, *Brandt and Chamberlain* [1959] were able to ignore hyperfine components because natural line broadening is much larger than the hyperfine splitting. Thus the Brandt and Chamberlain phase function,

$$\phi(\theta) = \tfrac{7}{6} - \tfrac{1}{4}\sin^2\theta, \tag{3}$$

is applicable to helium.

If the 30.4 nm column emission rate from the plasmasphere is measured and the solar flux is known, the column concentration of helium ions can be calculated from (1). The relationship between the column concentration and the number density of helium ions n_{He} at a given L shell and geocentric distance r is

$$N_{\mathrm{He}} = \int n_{\mathrm{He}}(r, L)\, ds(r, L), \tag{4}$$

where the integral is carried out along the LOS path $s(r, L)$ of the measurement. The various geometric conditions are contained within the coordinate system, the limits on the integrals, and the number density distribution.

The forward model is quite general and can be used for either "inside-out" viewing or to generate global images from a viewing perspective external to the plasmasphere. Since the number density description is a subroutine in the model code, it is easy to change from one type of distribution to another.

3.2. Parameterization of He^+ Concentration

The early parameterized model of *Meier and Weller* [1972] was based on a rather simplified description of in situ plasmaspheric ion measurements up to that time. The model was sufficient to demonstrate that the 30.4 nm emission observed from the early rockets and satellites [*Weller and Meier*, 1974] originated in the plasmasphere, but it was unable to reproduce details of the nighttime satellite data. As noted above, part of the difficulty was due to the contamination of the satellite signal near the magnetic equator. More recent parameterizations have been developed by *Gallagher et al.* [1988] and *Craven et al.* [1997]. The former utilizes nine parameters, and the latter is too elaborate for use with an inversion method. *Reynolds et al.* [1997] derived a kinetic description of the collisionless plasmasphere which we are currently studying for application to the plasmaspheric imaging problem. The approach taken here is to arrive at the minimum number of parameters for an adequate description of the plasmasphere and to evaluate the need for a more extensive model based on the STP analysis.

We have developed a new parameterization which is based on several sources of plasmaspheric information. The equatorial dependence of number density with L shell is obtained from the empirical expression derived by *Carpenter and Anderson* [1992] for the total electron density in a saturated plasmasphere

$$n_{\mathrm{apex}}(L) = n_0 10^{-aL}, \tag{5}$$

where the subscript "apex" indicates the apex of the field lines, the constant $a = 0.3145$, and n_0 is a constant to be determined from the data. As an initial value of n_0, we chose the Carpenter and Anderson normalization ($10^{3.9}$) divided by 10 to

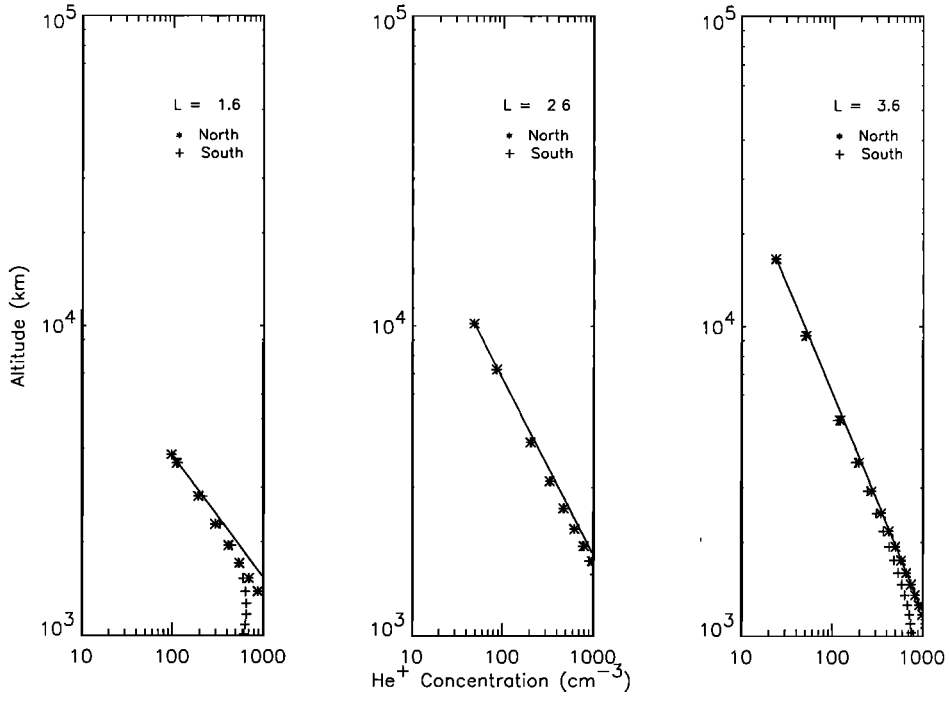

Figure 2. Comparison of He^+ number densities as functions of altitude along the indicated L shell. Individual points are from the field line interhemispheric plasmasphere (FLIP) model, and solid lines are from equation (6).

approximate the He^+ concentration. This value is further scaled as described below. We have used this function down to the ionosphere where it is merged with a Chapman layer to describe the ionospheric distribution of the plasmasphere. Details of the Chapman layer are not important to this work, since we focus on analysis of nighttime data where the ionosphere is not illuminated.

With data from the retarding ion mass spectrometer experiment on Dynamics Explorer DE 1, *Horwitz et al.* [1990] showed that He^+ closely tracked H^+ in the plasmasphere, so it appeared that use of (5) for helium as a proxy for the total plasma was justified. However, *Craven et al.* [1997], analyzing the same data set, found that the helium-to-hydrogen ratio does, indeed, vary with geocentric distance. The differences between these two analyses of the same data set has not been resolved. As a result, we keep a constant in this work, recognizing that future studies with better quality observations than STP 72-1 could allow for a to be retrieved from the data.

The ion concentration described at the field line apexes by (5) must now be mapped down to ionospheric altitudes. For guidance we turned to the field line interhemispheric plasmasphere (FLIP) model [e.g., see *Newberry et al.*, 1989, and references]. A series of FLIP simulations of plasmaspheric conditions appropriate to the STP 72-1 nighttime observations showed that the number density at night can be described by a power law in altitude z from the apex nearly down to the ionosphere:

$$n(z, L) = n_{\text{apex}}(L)(z_{\text{apex}}/z)^{\kappa(L)}, \qquad (6)$$

where the altitude at the apex of an L shell is $z_{\text{apex}} = R_E(L - 1)$ and R_E is the radius of the Earth. FLIP calculations showed that (6) departed from the numerical values near the ionosphere at high latitudes ($L \sim 4$). Again, this is not a significant issue for the nighttime observations. *Carpenter and Anderson* [1992] included a parameterization of the plasmapause L_{pp} which depends upon the geomagnetic index Kp. However we define the plasmapause L shell as a parameter to be retrieved from the data. The plasma trough description is that given by Carpenter and Anderson. The analysis is not sensitive to the magnitude of the trough value. The FLIP output indicated that the power κ of the density variation along the field line depends on L shell through the following relationship:

$$\log_e(\kappa) = \alpha[\log_e(L)]^2 + \beta[\log_e(L)] + \gamma, \qquad (7)$$

where α, β, and γ are parameters to be retrieved.

By combining (1)–(7), it is clear that the magnitude of the column emission rate in (1) depends linearly on the product of F_{Sun} and n_0; it is not possible to derive values for the two individually without independent information. Thus constant values are assumed for each, and a magnitude scalar of the intensity f is introduced as a parameter to be extracted from the data. Since the most important information expected from plasmaspheric imaging involves the dynamic response to geomagnetic forcing, the absolute values of the He^+ concentration are not of great significance [*Armstrong and Johnson*, 1995].

Note that there is no local time parameterization in this model. This is acceptable for the STP 72-1 nighttime analysis, since local solar time varies only by about 1 hour or less along the instrument LOS when sunlit at high altitudes. Also, the current parameterization does not include latitudinal asymmetries about the magnetic equator. Certainly, north/south asymmetries exist and should be parameterized in future work. The impact of this limitation on the present analysis will be addressed in section 5. Thus the model currently includes only the five parameters: L_{pp}, f, α, β, and γ.

Figure 2 compares the parameterized model with a FLIP run

Table 2. Solar-Geophysical Conditions for Selected Orbits

Orbit	Date	F_{10}	F_{10}^{ave}	Ap
603	Nov. 13, 1972	89	110	4
692	Nov. 19, 1972	102	110	11
1799	Feb. 4, 1973	97	101	7

appropriate to the conditions of STP 72-1 orbit 603 on November 13, 1972. The solar/geophysical conditions for orbit 603 and others discussed herein are listed in Table 2. The model parameters used were 3.7, 0.4, 0.175, −1.03, and 1.39 for L_{pp}, f, α, β, and γ, respectively. The FLIP results show a north/south asymmetry which is probably related to the higher ionization rate in the winter ionosphere. Clearly, the parameterized model provides a good fit to the FLIP values above the ionosphere and should contain sufficient flexibility to adjust for varying plasmaspheric conditions at night. (See section 5.4 for discussion of the daytime case.)

4. Discrete Inverse Theory

Before testing the forward model described in section 3, we describe the methodology for inverting data. The inversion process begins with discrete data, a parameterized forward model of those data, and a method of retrieving the parameters and their uncertainties from the data. In an ideal situation, complete orthogonal sampling of the plasmasphere would allow retrieval of the three-dimensional distribution of helium ions (tomography). Given the impracticality of this scenario, a priori information must be introduced in the form of a model (ideally based on physics) having parameters which can be retrieved from data. Our approach is to use the iterative maximum likelihood method [e.g., *Tarantola and Valette*, 1982; *Menke*, 1989], but we do not use the actual iterative formalism derived by those authors (as did *Meier and Picone* [1994]). Rather we employ the Levenberg-Marquardt (LM) method which is an efficient way of minimizing the generalized χ^2 (defined below). *Picone et al.* [1997a, b] have applied this technique to evaluate the retrieval of ionospheric parameters from OII 83.4 nm remote sensing data. *Press et al.* [1992] provide a good discussion of the LM method. A brief summary of the process follows, using the notation of *Menke* [1989]. More details are given by *Menke* [1989] and *Tarantola and Valette* [1982].

The forward model consisting of the combined optical and density models can be described by the following vector function **G**:

$$\mathbf{G}(\mathbf{m}) = \mathbf{d}^{pre}, \tag{8}$$

where **m** is a vector containing the model parameters (L_{pp}, f, α, β, and γ) and $\mathbf{d}^{pre}$ is a vector containing predictions of column emission rates corresponding to observed data. The vector function **G** maps the parameterized He^+ density distribution onto column emission rates. The maximum likelihood method maximizes the probability density Φ governing the relationships between the data and model parameters:

$$\Phi(\mathbf{m}^t, \mathbf{d}^t, \mathbf{d}^0) \propto P(\mathbf{d}^0|\mathbf{d}^t)P(\mathbf{d}^t|\mathbf{m}^t)P(\mathbf{m}^t, \langle\mathbf{m}\rangle). \tag{9}$$

In (9), $P(\mathbf{d}^0|\mathbf{d}^t)$ is the conditional probability that the observed column emission rates will be $\mathbf{d}^0$, given the true values $\mathbf{d}^t$; $P(\mathbf{d}^t|\mathbf{m}^t)$ is the conditional probability that the model **G** gives the true result $\mathbf{d}^t$ when the input parameters are $\mathbf{m}^t$; and $P(\mathbf{m}^t, \langle\mathbf{m}\rangle)$ describes the distribution of model parameters based on a priori or expected values $\langle\mathbf{m}\rangle$, which are derived from other sources. The two conditional probabilities allow for both random and systematic errors in the data and the model. The third probability density allows for the imposition of constraints from external information, a requirement when the problem is underdetermined or mixed-determined. Maximizing Φ is equivalent to minimizing χ^2. Assuming the instrument sensitivity is known, χ^2 is given as [*Picone et al.*, 1997b]

$$\chi^2 = (\mathbf{d}^0 - \mathbf{G}(\mathbf{m}))^T([\mathrm{Cov}\,\mathbf{d}^0] + [\mathrm{Cov}\,\mathbf{G}])^{-1}(\mathbf{d}^0 - \mathbf{G}(\mathbf{m})) + (\mathbf{m} - \langle\mathbf{m}\rangle)^T[\mathrm{Cov}\,\mathbf{m}]^{-1}(\mathbf{m} - \langle\mathbf{m}\rangle). \tag{10}$$

If the measurements are independent, the covariance matrix Cov $\mathbf{d}^0$ is diagonal with elements containing the variances of each measurement. (See *Menke* [1989] for definitions of the covariance matrices.) Uncertainties in the model are characterized by Cov **G** and uncertainties in the a priori model parameters $\langle\mathbf{m}\rangle$ are accounted for in Cov **m**. If no a priori information is available or necessary, Cov **m** may be considered as infinite, and the second term is zero. Minimizing χ^2 results in optimal estimates of the model parameters $\mathbf{m}^e$. The parameter uncertainties can be estimated, in analogy with the general linear Gaussian case, using the following expression for the covariance matrix which is a measure of the correlation among the retrieved parameters [*Menke*, 1989; *Tarantola and Valette*, 1982],

$$[\mathrm{Cov}\,\mathbf{m}^e] \cong \nabla\mathbf{G}^{inv}([\mathrm{Cov}\,\mathbf{d}^0] + [\mathrm{Cov}\,\mathbf{G}])(\nabla\mathbf{G}^{inv})^T + [\hat{\mathbf{I}} - \mathbf{R}] \cdot [\mathrm{Cov}\,\mathbf{m}][\hat{\mathbf{I}} - \mathbf{R}]^T = (\nabla\mathbf{G}^T([\mathrm{Cov}\,\mathbf{d}^0] + [\mathrm{Cov}\,\mathbf{G}])^{-1}\nabla\mathbf{G} + [\mathrm{Cov}\,\mathbf{m}]^{-1})^{-1}, \tag{11}$$

where $\hat{\mathbf{I}}$ is the identity matrix and **R** is the model resolution matrix [*Menke*, 1989]:

$$\mathbf{R} = \nabla\mathbf{G}^{inv}\nabla\mathbf{G}. \tag{12}$$

In (11) and (12), $\nabla\mathbf{G}^{inv}$ is the generalized inverse of $\nabla\mathbf{G}$, the matrix of partial derivatives of the model intensity with respect to each parameter evaluated at each data point. For overdetermined or exactly determined cases in which the model parameters are resolved, $\mathbf{R} = \hat{\mathbf{I}}$ and the a priori information contained in Cov **m** is irrelevant. For underdetermined or mixed-determined problems, $\nabla\mathbf{G}$ can have elements at or near zero, requiring the use of a priori information. As will be discussed in section 5.2, the behavior of **R** allows one to determine if a particular data set is sufficient to extract individual parameters of the model. For example, when $\mathbf{R} \neq \hat{\mathbf{I}}$, fidelity is lost in the retrieved parameters. (See chapter 4 of *Menke* [1989] for a discussion of the model resolution matrix.)

The diagonal elements of the covariance matrix are a measure of the width of the distribution of the retrieved parameters, and the off-diagonal elements indicate the degree to which pairs of parameters are correlated. Variance estimates for the retrieved model parameters can be obtained from the diagonal elements of Cov $\mathbf{m}^e$, and the standard deviation of m_i^e is $\sigma_i = (\mathrm{Cov}\,m_{ii}^e)^{1/2}$. Off-diagonal elements are related to the correlation coefficient between parameters, $r = \mathrm{Cov}\,m_{ij}/(\mathrm{Cov}\,m_{ii}\ \mathrm{Cov}\,m_{jj})^{1/2}$.

Uncertainties in helium ion densities computed from the model with the retrieved parameters and their uncertainties can now be calculated by propagation of errors [*Bevington and*

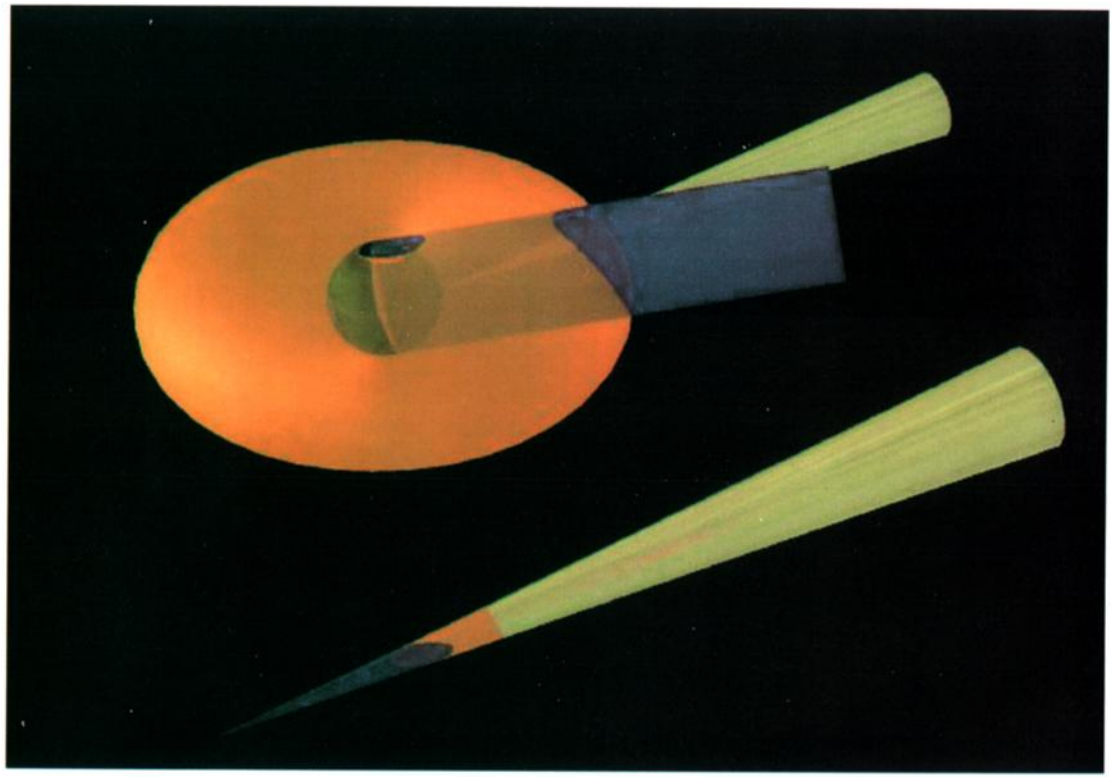

Plate 1. Three-dimensional visualization rendering of idealized plasmasphere on November 13, 1972 (orbit 603) with $L_{pp} = 4$. Sun shines from lower left to better view surface intersections along FOV. STP 72-1 instrument field of view is represented by a yellow cone. Note complex intersection of plasmasphere with Earth shadow. Expanded view of intersection of the instrument field of view and shadow is shown at the bottom.

Robinson, 1992]. The variance, "var," of the He^+ concentration at altitude z along a given L shell is given by

$$\text{var}\,[n_{\text{He}}(z, L)] \cong \sum_i \sum_j [\text{Cov}\,\mathbf{m}^e]_{ij} \cdot \left(\frac{\partial n_{\text{He}}(z, L)}{\partial \mathbf{m}_i}\right)^e \left(\frac{\partial n_{\text{He}}(z, L)}{\partial \mathbf{m}_j}\right)^e, \quad (13)$$

where, again, the superscript indicates evaluation at the estimated model parameters returned in the retrieval process. More detailed discussion of (8)–(13) is provided by *Picone et al.* [1997b].

5. Analysis of Selected Orbits

5.1. Visualization

Remote sensing of the plasmasphere from LEO poses a formidable obstacle to visualization of the region being sampled. Especially difficult is the night sector where the detector LOS begins at the satellite, progresses through the shadow, breaks into sunlight (unless pointed directly down the shadow), and encounters scattering from sunlit helium ions. As STP 72-1 moved around Earth, the volume of plasma sensed changed dramatically, causing variations of the nighttime intensity profiles in ways which are not intuitive (see Figure 1).

In order to visualize the complex geometrical influences of the sensor LOS, the shadow, and the plasmapause, we developed a three dimensional imaging approach using Strata StudioPro™. An example of the complex geometry encountered when viewing within the Earth shadow is illustrated in Plate 1. The plasmasphere is rendered as a torus-like translucent solid created by rotating a dipole around Earth. The outer surface represents the plasmapause at $L_{pp} = 4$. The Sun shines from the left producing the cylindrical shadow projected to the right. A small amount of secondary (artificial) lighting is used to highlight the three-dimensional character of the plasmasphere. Viewing conditions are illustrated for STP 72-1 at the equator during orbit 603 on November 13, 1972. Note the complex intersection of the plasmapause and the shadow due to the southern hemispheric location of the subsolar point. Plasmaspheric shadowing in the polar regions is complicated as well. The STP 72-1 instrumental FOV is a right conic section, shown in yellow outside the plasmasphere. The translucent plasmasphere permits visualization of the region of sunlit helium ions being detected between the shadow and the plasmapause. The FOV cone is expanded for better viewing in the bottom of Plate 1.

Plate 2 displays viewing conditions for 12 orbital locations of orbit 603 in order to illustrate the changing illumination conditions. For these images the Sun is to the right to better see the FOV exiting the shadow and plasmapause during the night. During the day the instrument views the topside ionosphere and the plasmasphere. Little emission is expected over the polar regions because of the lack of plasma confinement by the magnetic field; this is faithfully rendered by the geometry. At night the emission rate rises (Figure 1) as the LOS crosses into the sunlit plasmasphere (Plate 2) but then decreases as the shadow-plasmapause intersection moves to higher altitudes.

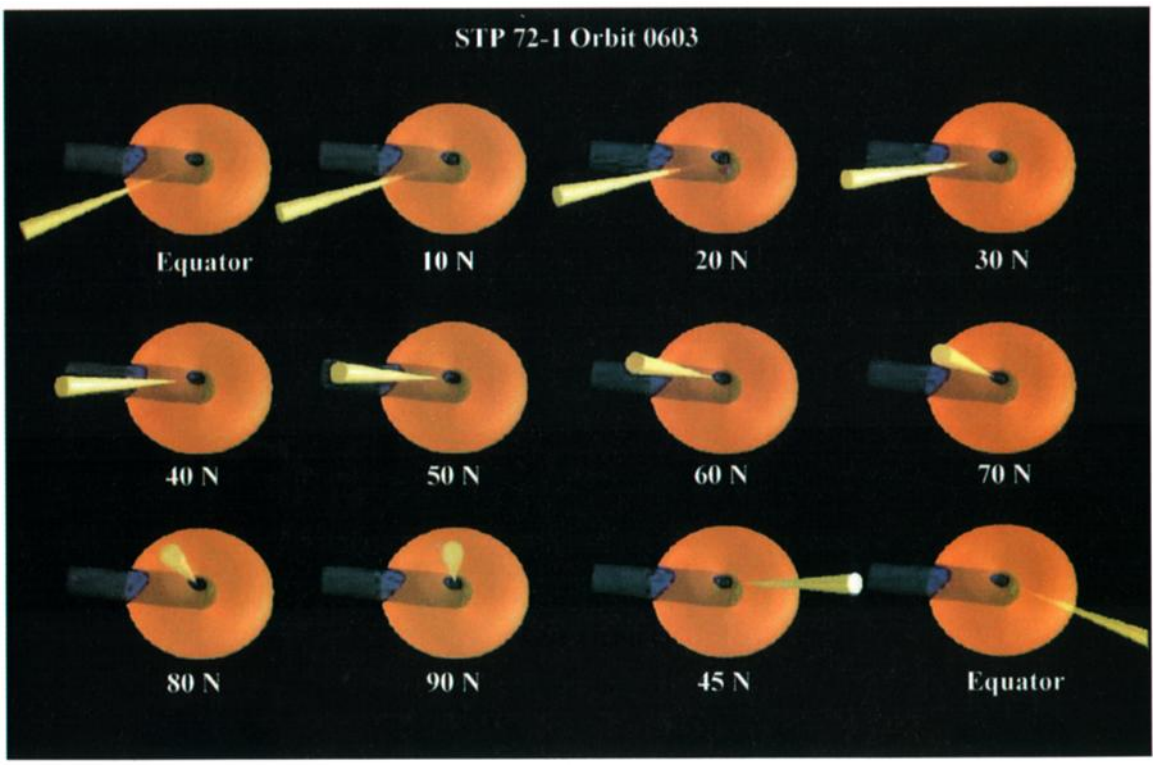

Plate 2. Three-dimensional visualization of regions of plasmasphere viewed by STP 72-1 instrument for selected orbital locations of orbit 603. $L_{pp} = 4$. These images have the Sun to the right for better viewing of the FOV intersection with the shadow/plasmapause.

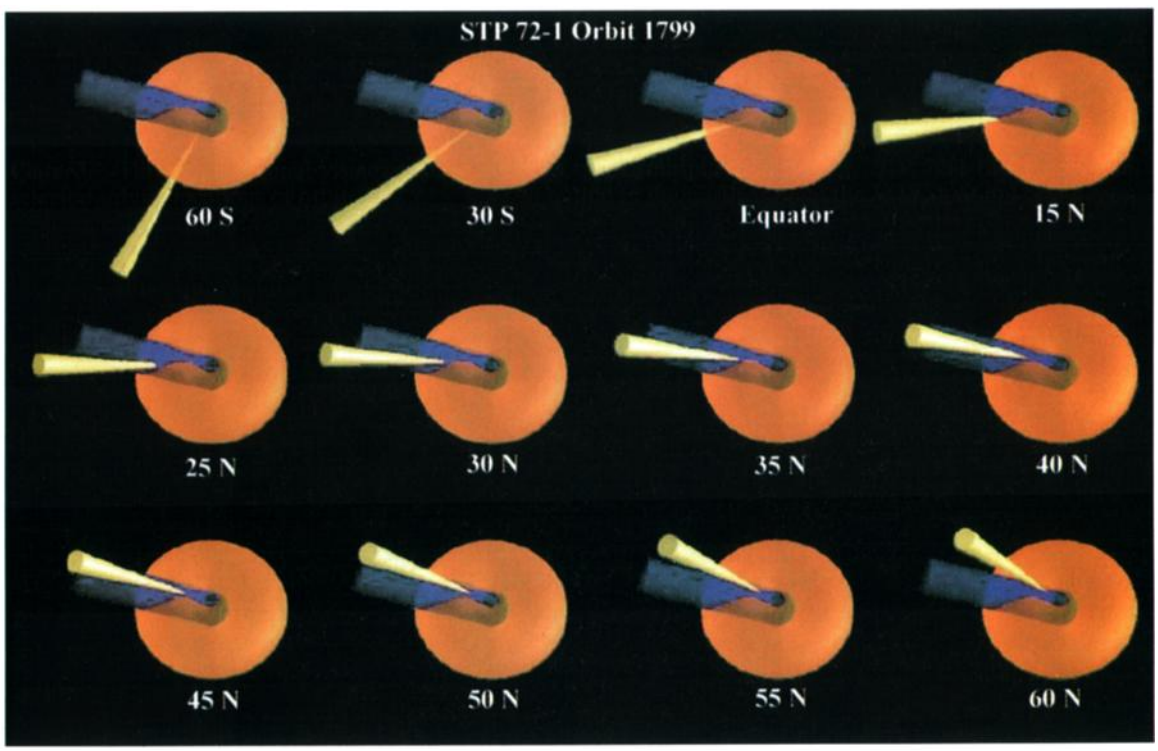

Plate 3. Three-dimensional visualization of regions of plasmasphere viewed by STP 72-1 instrument for selected orbital locations of orbit 1799. $L_{pp} = 4$. Note that in the north at night the FOV does not break into sunlight until well beyond $L = 4$.

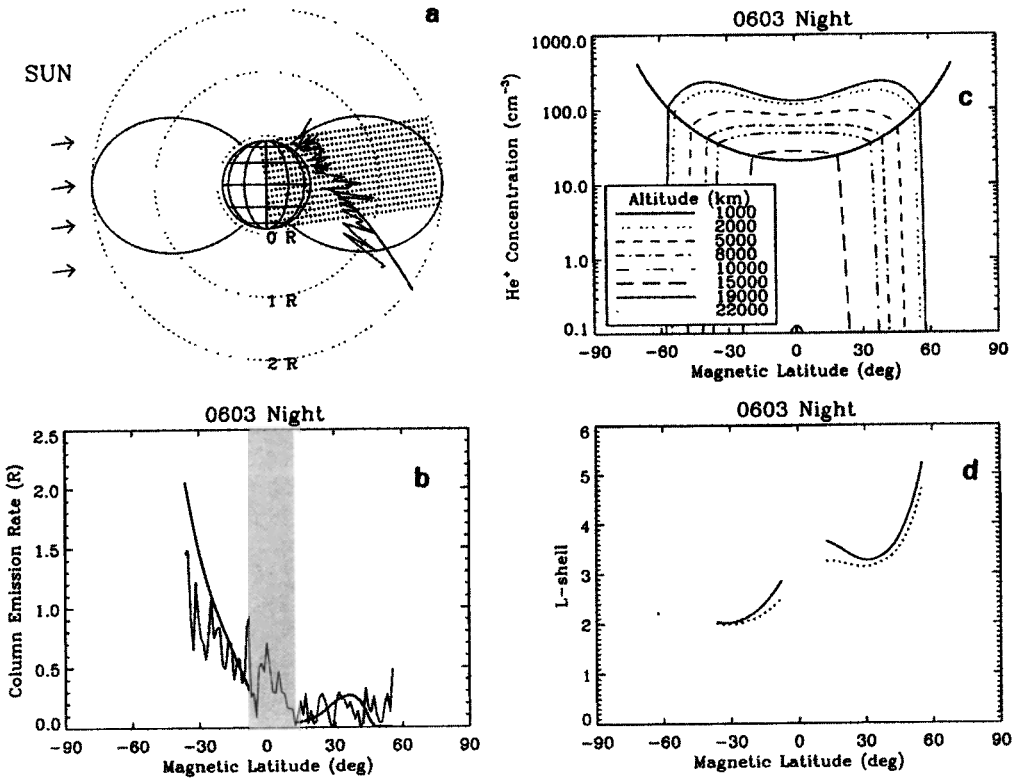

Figure 3. Comparison of model emission rates using concentrations shown in Figure 2 to nighttime data from orbit 603 on November 13, 1972. (a) Equatorial plot as described in Figure 1 caption. Model results are shown by smooth curve. (b) Model-data comparison in rectilinear format. The shaded region covers contaminated data which were not included in the analysis (see text). Individual data points connected by dotted line. (c) He^+ concentrations versus magnetic latitude for selected altitudes. (d) L shell where instrument line of sight (LOS) breaks into sunlight. The solid curve gives the L shell of the center of the instrument FOV, while the dotted curve indicates the lowest sunlit L shell which is seen within the full 9° FOV.

Minimum intensity occurs at the closest approach of the LOS to the antisolar direction.

5.2. Night Observations

As mentioned above, we focus the analysis on selected nighttime orbits of STP 72-1. We begin by showing in Figure 3 a comparison of the observations and a forward calculation with the model parameters used in Figure 2, $\mathbf{m}^e = [L_{pp}, f, \alpha, \beta, \gamma] = [3.7, 0.4, 0.175, -1.03, 1.39]$. Figure 3a shows a polar-style plot, Figure 3b contains a rectilinear plot, Figure 3c displays the model densities, and Figure 3d contains a plot of the L shell where the instrument LOS breaks into sunlight. Note that data near the magnetic equator in Figure 3b have been shaded to indicate the region of contamination described in section 2. Although the model emission rates have been integrated over the full instrumental FOV, they differ little from those computed with a single LOS. The emission rates are higher in the southern hemisphere at night since that part of the plasmasphere receives greater illumination in November. While the magnitudes of the observed and modeled intensities are similar, the variations with latitude (and angle from the Sun) are somewhat different.

The DIT inversion procedure is now employed to see if the fit to the data shown in Figure 3 can be improved. We start by using the model parameters for the FLIP case as initial values. No a priori information was invoked. Contaminated data in the shaded region of Figure 3b were not included in the inversion analysis. Convergence was achieved after five iterations, using the criteria that the change in χ^2 is less than 10^{-3} for successive iterations. The actual value of the reduced χ^2 is 1.5, suggesting that a somewhat better fit is possible. The probability Q that the value of χ^2 is larger than 1.5 based on random chance alone is about 0.002 in support of that hypothesis [*Press et al.*, 1992, pp. 654 and 658]. The resulting estimated parameters are $\mathbf{m}^e = [3.70, 0.364, 0.913, -5.66, 4.10]$ with uncertainties of $\sigma = [0.0142, 0.0378, 0.395, 1.36, 1.08]$, respectively. Comparison of the model with the data is shown in Figure 4. Clearly, the retrieved parameters provide much better agreement with the data than do the FLIP-equivalent values in Figure 3. The low values of σ_1 and σ_2 for L_{pp} and f, respectively, imply that those parameters are retrieved with high accuracy. However, the larger values of σ_i for the remaining parameters are evidence that we have not been able to retrieve precise values from the STP 72-1 data set.

Although there are difficulties with the results of the analysis of orbit 603, we have, nonetheless, achieved our initial goal of demonstrating that the nighttime data can be fit with a model of the plasmasphere (at least where contamination is not a problem). Thus we have satisfied a necessary condition of the model but have not established sufficiency.

A second example is shown in Figure 5 for orbit 692 on November 19, 1972. Again, the fit to the data appears to be quite good. The retrieved parameters are $\mathbf{m}^e = [4.00, 0.0979, 1.28, -3.47, 2.81]$ with uncertainties of $\sigma =$

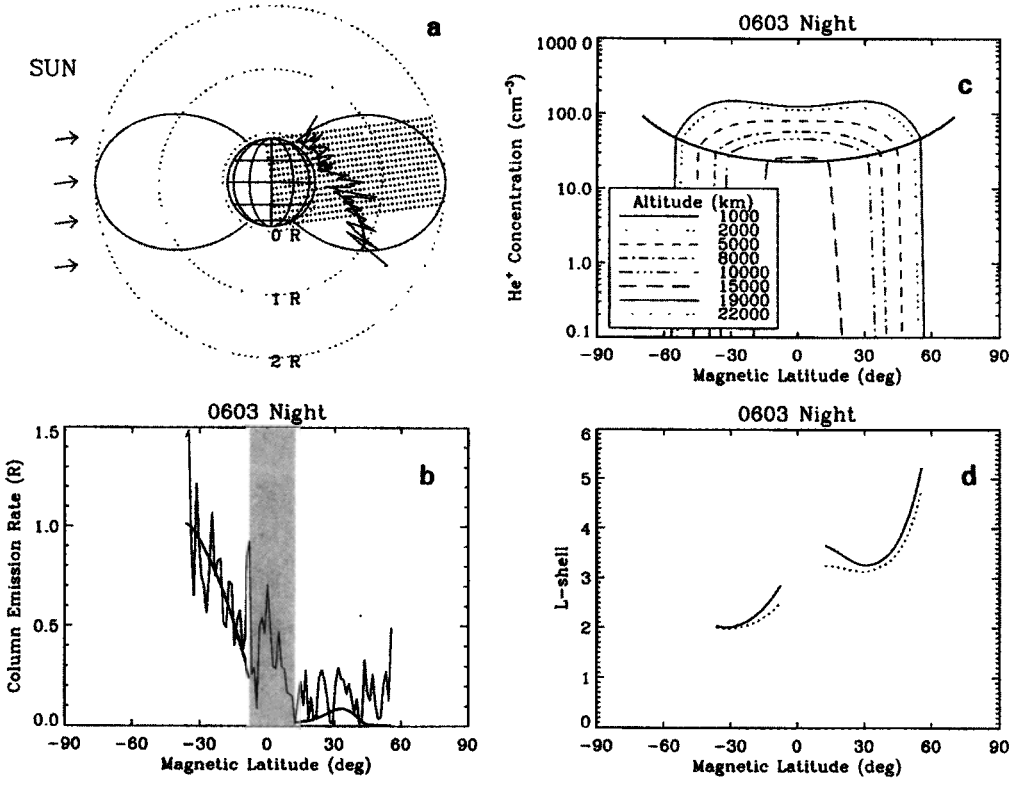

Figure 4. Comparison of data from orbit 603 with model emission rates using retrieved parameters. (a) Equatorial plot. (b) Model-data comparison in rectilinear format. (c) He^+ concentrations versus magnetic latitude for selected altitudes. (d) L shell where instrument LOS breaks into sunlight. See Figure 3 caption.

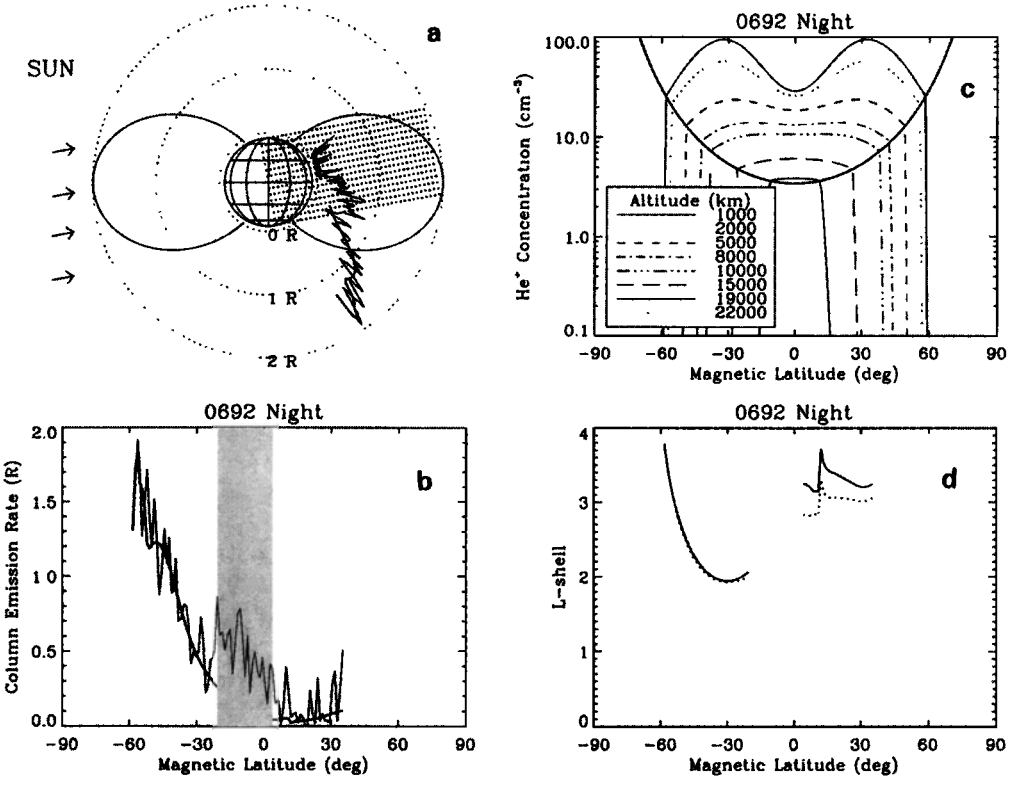

Figure 5. Same as Figure 4, except for orbit 692 on November 19, 1972.

Table 3. Diagonal Elements of Model Resolution Matrix **R**

Case	Condition	Data*	R_{11}, L_{pp}	R_{22}, f	R_{33}, α	R_{44}, β	R_{55}, γ
Orbit 603	observed	A	0.998	0.949	0.015	0.280	0.502
Orbit 603	low-noise data	S	0.999	0.999	0.207	0.856	0.929
Sky scan	0° latitude	S	1.00	1.00	0.644	1.25	1.14
Sky scan	0° and 50° latitude	S	1.00	1.00	1.01	0.910	0.952

*A, actual data; S, synthetic data.

[0.0523, 0.0128, 0.326, 0.728, 0.409], respectively, and the reduced χ^2 is 1.2. The value of Q is 0.05, indicating that an acceptable fit has been achieved. As in orbit 603, the values of σ_i are low for the first two parameters and are high for the remainder. Similar results were found for data from the other orbits as well. Inversions of data from two other orbits were aborted because of a matrix inversion error. This was caused by insensitivity of the observations to one or more model parameters, so that the partial derivative matrix is singular, and the problem is underdetermined or at least mixed-determined. Imposing a priori constraints (e.g., plasmapause is required to be between 2 and 7, and magnitude scalar is positive definite) rendered the inversion stable.

As discussed in section 4, a number of tests are available for investigating the quality of the retrieved parameter values and hence the information content of the STP 72-1 data. The first is the basic reproducibility test to see if the estimated parameters could be consistently returned using different initial guesses of parameter values. (We avoid using the often misapplied term "uniqueness." Since uncertainties are present in both the observations and the model, it is not possible to demonstrate uniqueness. However, a robust inversion problem must be able to produce values of the parameters to within their uncertainties.) We found that the values of $\mathbf{m}^e$ returned from case to case varied by more than their 1σ values, depending upon the initial guess, even though values of χ^2 were comparable.

The second test explores the properties of the model resolution matrix **R** which characterizes the relationship between $\mathbf{m}^e$ and the "true" parameter values $\mathbf{m}^t$, which best describe the plasmaspheric state underlying the data. This is clearly seen in the ideal linear case [*Menke*, 1989], where $\mathbf{m}^e = \mathbf{R}\mathbf{m}^t$. When $\mathbf{R} = \hat{\mathbf{I}}$, $\mathbf{m}^e = \mathbf{m}^t$, and each parameter is resolved by the data set. **R** can be considered a filter of the "true" model parameters by the given observational approach. Even though true model parameters are usually not known when inverting actual data, **R** still provides a very useful indicator. The diagonal elements of the model resolution matrix for the retrieval applied to orbit 603 were diagonal (diag) **R** = [0.998, 0.949, 0.0146, 0.280, 0.502]. Similar values were obtained for the

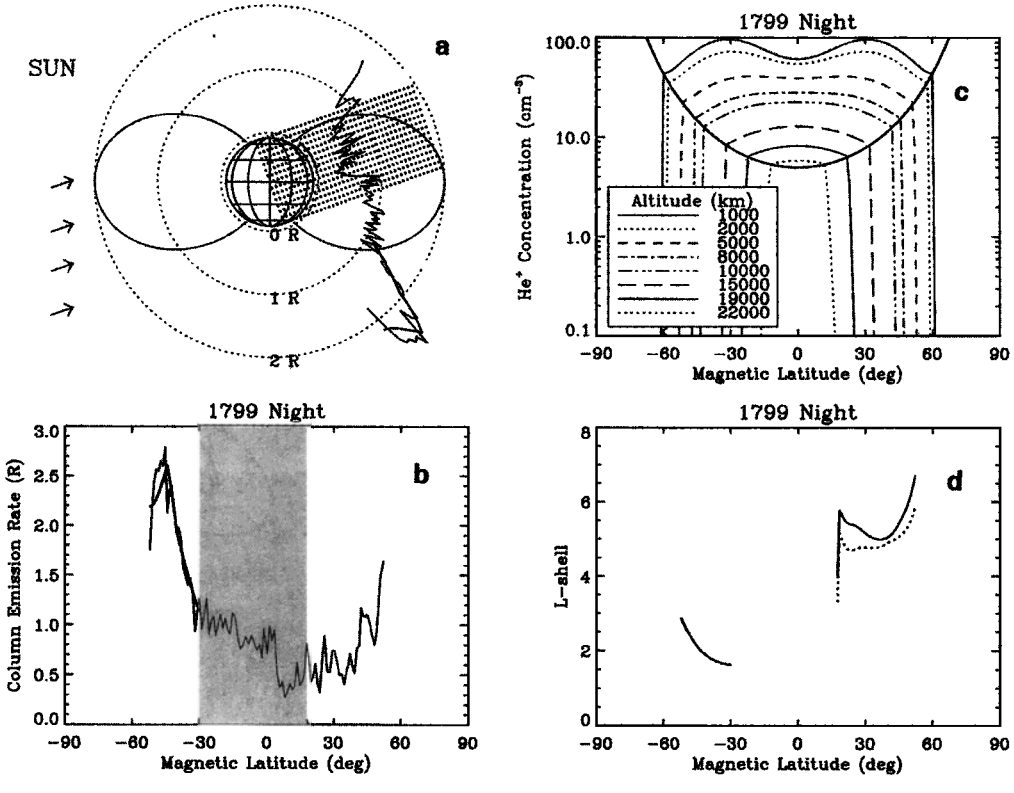

Figure 6. Comparison or data from nighttime portion of orbit 1799 on February 4, 1973, with model emission rates using retrieved parameters. (a) Equatorial plot. (b) Model-data comparison in rectilinear format. (c) He^+ concentrations versus magnetic latitude for selected altitudes. (d) L shell where instrument LOS breaks into sunlight.

other passes. This is an indication that parameters of the model, other than f and L_{pp}, might not be resolvable with the STP 72-1 observational approach.

A third related test is to examine the correlation matrix. If the parameters are nearly orthogonal, the correlation coefficient between individual parameters should be near zero. Often, the correlation coefficient between pairs of α, β, or γ was found to be moderate or high, supporting the notion that the parameters are interdependent and therefore difficult to resolve.

There are at least three possible reasons for the ambiguities in α, β, and γ: (1) there is too much noise in the data; (2) the observational sampling is inadequate (i.e., the problem is underdetermined or mixed-determined); and (3) the parameterization of the helium number density is inappropriate for representing the plasmaspheric properties being sensed by the experiment. We examine these in detail next, using the model resolution matrix as the chief diagnostic.

5.2.1. Noisy data. To test the effect of counting statistics on the retrieval problem, we created synthetic data using the retrieved parameters for orbit 603. The process consists of using the forward model to compute column emission rates for each of the observing locations and directions. Statistical noise is then added by converting the emission rates into counts, calculating the standard deviation of each point, combining with a set of normally distributed random numbers, superimposing the noise onto the computed intensity, and then converting back to Rayleighs. In this case and those which follow, the "true" model parameters, $\mathbf{m}'$ are known. For the present example, an "instrument" calibration factor of 10^7 counts Rayleigh^{-1} was employed to minimize the effect of noise. The comparison between diag **R** for the retrieval using the actual data and the synthetic data with low noise is shown in the upper part of Table 3. The first row shows R_{ii} for the observed data from orbit 603, and the second row shows R_{ii} for the low-noise synthetic data. Although there is some increase toward unity in the diagonal values corresponding to α, β, and γ, the parameters are still unresolved. The correlation between parameters also remains high. We conclude that although poor counting statistics contribute to the parameter resolution problem, it is not the sole source.

5.2.2. Inadequate sampling: Comparison with multipoint observing. To test this hypothesis, we consider how the sampling would improve the resolution of parameters if the full spin-scan data were still available. We first constructed a set of 62 synthetic data points for a single sky scan in the orbital plane from horizon through zenith and back to the opposite horizon. The spacecraft was located at the antisolar point of orbit 603. Again, the high "instrument" sensitivity was used in constructing the data to avoid the effect of counting statistics. The model resolution matrix diagonal elements from the inversion of the single sky scan are shown as the third row of Table 3. There is some improvement in R_{33}, but R_{44} and R_{55} are comparable to those obtained from the simulation of STP 72-1 (second row of Table 3). Thus a single sky scan is not much better than an orbital pass with near-zenith viewing.

Next, synthetic data from a second sky scan were created in this case with the observing site at 50° latitude. The two sky scans were then inverted together as a single data set to study the effect of multipoint viewing. Values of diag **R** are shown as the last row in Table 3. The values of R_{ii} are much closer to unity, showing a significant improvement in the ability to resolve the model parameters. We conclude that the observations made around the orbit in the near-zenith direction are not sufficient to extract parameters of the present model but that sky scans from multiple observing sites would be sufficient to do so.

5.2.3. Model parameterization. The results of our tests described earlier and the improvement realized by adding a second simultaneous (simulated) observation set strongly indicate that the STP 72-1 data provide useful information on the global plasmaspheric parameters L_{pp} and f but do not contain sufficient information to determine the internal structure, that is, the dependence of the He^+ density on L. For this reason we have not investigated different forms of the L dependence except for a linear form of (7), which proved to be unsatisfactory. Without local time, latitude, and longitude parameterizations the present model has severe limitations. It is possible that a functional form more strongly based on physics would provide a much better representation of the plasmasphere without running into the problems of parameter resolution. We are currently investigating application of a new first-principles model to the inversion problem [*Reynolds et al.*, 1997]. It is unlikely that the limited information from the STP 72-1 data would be sufficient to completely specify the parameters of any alternative model.

Because of the difficulties encountered in resolving the model parameters, we do not present uncertainties in the He^+ concentrations shown in Figures 4 and 5. They are large (a few percent to more than 100%), reflecting the propagation of the retrieved parameter uncertainties (equation (13)).

5.3. Detection of He^+ Outside of Plasmasphere

On February 4, 1972, two contiguous full orbits of data were obtained. The inversion process was applied to them with rather startling results. Figure 6 shows the comparison of the retrieved model with the data for the nighttime portion of orbit 1799. The retrieved value of L_{pp} for orbit 1799 is 3.78. The model does a reasonable job of matching the southern observations but predicts nearly zero emission rate in the north. A study of the observing geometry illustrates why. The images in Plate 3 reveal that the instrument FOV remains within the Earth shadow throughout the northern part of the orbit. That is, the FOV breaks into sunlight only beyond the plasmapause, beginning at about $L = 5.5$ (see Figure 6d). Thus the emission rate in the north is coming from outside the plasmasphere proper as modeled.

Because the emission covers some 30° of latitude, the glowing plasma would be about 3 R_E in north-south extension if it were located at 6 R_E geocentric distance (ignoring any magnetic field geometry). The He^+ column concentration can be estimated from (1). The 30.4 nm g factor for solar minimum conditions is 1.84×10^{-5} s^{-1} [*Meier*, 1991]. (Note that the value in Table IV of *Meier* [1991] is low by a factor of 2, an error traceable to the fact that the line profile used to compute the line-center flux was plotted with a second-order wavelength scale by *Doschek et al.* [1974].) Using the *Hinteregger et al.* [1981] solar proxy model for February 4, 1972, we calculate $g = 2.7 \times 10^{-5}$ s^{-1}. For an emission rate of 0.5 R, the column concentration $N_{He} = 1.8 \times 10^{10}$ ions cm^{-2}. An estimate of the size of the emitting region is needed to calculate number densities. The data of *Moldwin et al.* [1995] and *Ober et al.* [1997] indicate cold plasma regions of the order of 1 R_E or greater at geosynchronous altitude. If the thickness of the emitting region were 1 R_E, the average number He^+ density would be about 30 cm^{-3}. If the He^+/H^+ ratio were known, we could estimate the electron density ($H^+ + He^+$). For a helium

to hydrogen ratio of 0.2 the electron density is about 170 cm^{-3}. However, if the ion ratio were 0.4 and the emitting region covered 2 R_E, the electron density would be about 50 cm^{-3}. Both of these estimates are larger than the typical observed electron densities beyond the plasmapause of less than 10 cm^{-3} [*Carpenter and Anderson*, 1992], although *Moldwin et al.* [1995] report occasional observations of electron densities at geosynchronous altitude which are consistent with our lower estimates.

The northern data in Figure 6 suggest that the plasmapause has contracted, freeing plasma to move outward toward the magnetopause. Evidence for such movement of cold plasma at geosynchronous orbit, both at dusk and in the premidnight sector, has been reported by *Moldwin et al.* [1995, 1996], *Weiss et al.* [1997], and *Ober et al.* [1997]. In those experiments the near-midnight phenomena appears to be associated with the growth phase of a geomagnetic substorm following an extended period of low magnetospheric activity. Our conditions are different: geomagnetic activity on the day of and before orbit 1799 was not particularly significant ($-25 < DST < -4$; $Kp < 4$). In fact, this is consistent with the findings of *McComas et al.* [1993] and *Moldwin et al.* [1994] that for low levels of magnetic activity ($Kp \leq 2$), regions of cold plasma at geosynchronous orbit could be observed at any local time. *McComas et al.* [1993, Figure 6d] show one example of cold plasma present at high altitude on March 3, 1992, when Kp ranged from 2− to 3+. The plasma was highly variable, expanding and contracting at various local times, even close to 0100 LT. Our results in Figure 6 confirm the qualitative conclusion that the plasmapause is not necessarily well defined when Kp is small. Unfortunately, the present observations are not detailed enough nor numerous enough to shed further light on the specific nature of this region of the magnetosphere. However, future experiments imaging the plasmasphere from an external high-altitude location will provide unambiguous views of the structure and dynamics of plasma at and beyond the plasmapause.

5.4. Daytime Observations

STP 72-1 observations during the day from 740 km contain He^+ EUV emission from both the ionosphere and the plasmasphere. In order to obtain an estimate of the relative contributions from these regions, we carried out FLIP calculations corresponding to the November 1972 period. The resulting He^+ concentrations did not follow the simple power law found for night conditions (equation (6)). Rather, two peaks were found in the variation of concentration with altitude along a field line, one in the ionosphere and the other at a few thousand kilometers. Similar results were reported by *Newberry et al.* [1989] for the case when the photoelectron energy loss in the plasmasphere was set at 55% (the value used in the present calculations as well). Significant differences were seen between the northern and southern distributions in our FLIP runs, again reflecting the higher photoionization rate of helium atoms due to the northern winter neutral helium bulge.

Here we assess the ability to differentiate the ionospheric and plasmaspheric contributions to the daytime STP 72-1 signals. On the basis of our nighttime study, we conclude that the data do not contain sufficient information to warrant developing a complex parameterization of the daytime He^+ concentration for similar inversion studies. Fortunately, a qualitative assessment requires only the evaluation of the column emission rate along two lines of sight corresponding to northern and southern magnetic latitudes. Here we have chosen ±43.1° magnetic latitude ($L = 2.1$ at 740 km). The column concentration was calculated with FLIP for various distances along the lines of sight and converted to emission rate via (1). In the south, 50% of the column emission rate originated between 740 and 2200 km. In the north the 50% altitudes were 740 and 1800 km. We conclude that the daytime emission rate is significantly influenced by ionospheric plasma and that a single detector viewing radially outward from LEO provides inadequate data for discriminating between the high-altitude (plasmaspheric) and low-altitude (ionospheric) sources.

6. Discussion and Conclusions

We have demonstrated that the STP 72-1 satellite observations of the plasmasphere using EUV remote sensing can now be well fitted with a simple parameterized model based on a first-principles approach (FLIP). Earlier problems with primitive plasmasphere models and contamination of the data by emissions, apparently from ring current neutral particles, have been overcome. A new powerful method of inverting remote sensing data has been developed and applied to the STP data. Within this framework, tools are available for investigating the quality of the retrieved model parameters and diagnosing problem areas in the data interpretation. Analysis of a number of orbits of STP data shows that the data can be reproduced by the model to well within the statistical uncertainty and that global model parameters (L_{pp} and f) can be retrieved satisfactorily. However, sampling of the plasmasphere with only near-zenith observations is inadequate for determining internal plasmaspheric structure. He^+ number densities retrieved from the EUV data are not of sufficient precision to provide quantitative tests of plasmaspheric models such as FLIP. Alternatively, tests with synthetic data show that spin-scan data from multiple observing locations would, indeed, provide sufficient observational sampling to resolve both global and structural parameters of the current model. We believe that combining simultaneous LEO and high Earth orbit imaging data would constitute a powerful means of obtaining quantitative knowledge of the plasmasphere on a global scale.

While observing the plasmasphere from LEO poses formidable problems in visualization, a significant step forward has been made with the development of a new three-dimensional imaging system. This "cartoon-like" approach enables rapid appraisal of the plasmaspheric region being detected and should prove to be an effective tool for planning of future missions. Video simulations are easily created and aid visualization tremendously. Noteworthy is its application to the STP 72-1 observations on February 4, 1973, where a major disagreement between the data and the model is apparent. On the basis of the geometric considerations alone, the three-dimensional imaging system quickly demonstrated that the emitting region had to reside beyond the plasmapause. Our estimates of the electron densities are roughly consistent with occasional observations of cold plasmaspheric plasma at geosynchronous altitude. Apparently, the plasmapause contains structure, even under conditions of low geomagnetic activity.

The next step in evaluating EUV remote sensing is to apply DIT to the external viewing case. This is straightforward for single sky scans, but significant computational barriers arise with the large number of pixels present in an image. More degrees of freedom will be needed in the models. We also intend to explore the advantages of multipoint imaging from

two or more viewing perspectives. The tools developed in this work will aid tremendously in evaluating observational scenarios which are needed to remove ambiguities, to eliminate underdetermined or mixed-determined problems in the image inversion process, and to provide accurate model parameters and plasmaspheric He^+ number densities.

Acknowledgments. We thank G. R. Gladstone for arranging the digitization of the STP 72-1 strip charts and Barry H. Mauk for discussions about inverse theory. Ronald Thomas supplied the Levenberg-Marquardt minimization software. Charles Weller was the principal investigator of the NRL experiment on STP 72-1. Partial support of the NRL authors was provided by the Office of Naval Research. R. R. Meier also received partial support from NASA grant W-19103 (Multi-Point Magnetospheric Reconnaissance Imaging). G. Ganguli and D. Melendez-Alvira received partial support from NASA grant W-19269 (Plasmasphere Morphology and Dynamics: A Multi-Species Kinetic Model). E. C. Roelof received partial support from NASA grant NAGW-2691.

The Editor thanks Supriya Chakrabarti and another referee for their assistance in evaluating this paper.

References

Anderson, D. E. Jr., R. R. Meier, and C. S. Weller, Observations of far and extreme ultraviolet OI emission in the tropical ionosphere, *Planet. Space Sci.*, *24*, 945, 1976.

Armstrong, T. P., and C. L. Johnson, Magnetosphere imager science definition team interim report, *NASA Ref. Publ. 1378*, Marshall Space Flight Cent., Huntsville, Ala., 1995.

Bevington, P. R., and D. K. Robinson, *Data Reduction and Error Analysis for the Physical Sciences*, 2nd ed., McGraw-Hill, New York, 1992.

Brandt, J. C., and J. W. Chamberlain, Interplanetary gas, I, Hydrogen radiation in the night sky, *Astrophys. J.*, *130*, 670, 1959.

Carpenter, D. L., and R. R. Anderson, An ISEE/whistler model of equatorial electron density in the magnetosphere, *J. Geophys. Res.*, *97*, 1097, 1992.

Chakrabarti, S., F. Paresce, S. Bowyer, Y. T. Chiu, and A. Aikin, Plasmaspheric helium ion distribution from satellite observations of He II 304 Å, *Geophys. Res. Lett.*, *9*, 151, 1982.

Craven, P. D., D. L. Gallagher, and R. H. Comfort, Relative concentration of He^+ in the inner magnetosphere as observed by the DE 1 retarding ion mass spectrometer, *J. Geophys. Res.*, *102*, 2279, 1997.

Doschek, G. A., W. E. Behring, and U. Feldman, The widths of the solar He I and He II lines at 584, 537, and 304 Å, *Astrophys. J.*, *190*, L141, 1974.

Gallagher, D. L., P. D. Craven, and R. H. Comfort, An empirical model of the Earth's plasmasphere, *Adv. Space Res.*, *8*(8), 15, 1988.

Hinteregger, H. E., K. Fukui, and B. R. Gilson, Observational, reference and model data on solar EUV, from measurements on AE-E, *Geophys. Res. Lett.*, *8*, 1147, 1981.

Horwitz, J. L., R. H. Comfort, and C. R. Chapell, A statistical study of plasmasphere density structure and boundary locations, *J. Geophys. Res.*, *95*, 7937, 1990.

Jelinsky, P., J. V. Vallerga, and J. Edelstein, First spectral observations of the diffuse background with the Extreme Ultraviolet Explorer, *Astrophys. J.*, *442*, 653, 1995.

Johnson, C. Y., J. M. Young, and J. C. Holmes, Magnetoglow: A new geophysical resource, *Science*, *171*, 379, 1971.

McComas, D. J., S. J. Bame, B. L. Barraclough, J. R. Donart, R. C. Elphic, J. T. Gosling, M. B. Moldwin, K. R. Moore, and M. F. Thomsen, Magnetospheric plasma analyzer: Initial three-spacecraft observations from geosynchronous orbit, *J. Geophys. Res.*, *98*, 13453, 1993.

Meier, R. R., Ultraviolet spectroscopy and remote sensing of the upper atmosphere, *Space Sci. Rev.*, *58*, 1, 1991.

Meier, R. R., and J. M. Picone, Retrieval of absolute thermospheric concentrations from the far UV dayglow: An application of discrete inverse theory, *J. Geophys. Res.*, *99*, 6307, 1994.

Meier, R. R., and C. S. Weller, EUV resonance radiation from helium atoms and ions in the geocorona, *J. Geophys. Res.*, *77*, 1190, 1972.

Meier, R. R., and C. S. Weller, Extreme ultraviolet observations of the latitudinal variation of helium, *J. Geophys. Res.*, *79*, 1575, 1974.

Meier, R. R., and C. S. Weller, Observations of equatorial EUV bands—Evidence for low-altitude precipitation of ring current helium, *J. Geophys. Res.*, *80*, 2813, 1975.

Menke, W., *Geophysical Data Analysis: Discrete Inverse Theory, Int. Geophys. Ser.*, vol. 45, Academic, San Diego, Calif., 1989.

Moldwin, M. B., M. F. Thomsen, S. J. Bame, D. J. McComas, and K. R. Moore, The structure and dynamics of the outer plasmasphere: A multiple geosynchronous satellite study, *J. Geophys. Res.*, *99*, 11475, 1994.

Moldwin, M. B., M. F. Thomsen, S. J. Bame, and D. McComas, The fine-scale structure of the outer plasmasphere, *J. Geophys. Res.*, *100*, 8021, 1995.

Moldwin, M. B., M. F. Thomsen, S. J. Bame, D. J. McComas, and L. A. Weiss, The appearance of plasmaspheric plasma in the outer magnetosphere in association with the substorm growth phase, *Geophys. Res. Lett.*, *23*, 801, 1996.

Newberry, I. T., R. H. Comfort, P. G. Richards, and C. R. Chappell, Thermal He^+ in the plasmasphere: Comparison of observations with numerical calculations, *J. Geophys. Res.*, *94*, 15265, 1989.

Ober, D. M., J. L. Horwitz, M. F. Thomsen, R. C. Elphric, D. J. McComas, R. D. Belian, and M. B. Moldwin, Premidnight plasmaspheric "plumes," *J. Geophys. Res.*, *102*, 11325, 1997.

Paresce, F., S. Bowyer, and S. Kumar, On the distribution of He^+ in the plasmasphere from observations of resonantly scattered He II 304-Å radiation, *J. Geophys. Res.*, *79*, 174, 1974.

Paresce, F., H. Fahr, and G. Lay, A search for interplanetary He II, 304-A emission, *J. Geophys. Res.*, *86*, 10038, 1981.

Picone, J. M., R. R. Meier, O. A. Kelley, D. J. Melendez-Alvira, K. F. Dymond, and R. P. McCoy, Discrete inverse theory for 834-Å ionospheric remote sensing, *Radio Sci.*, *32*, 1973, 1997a.

Picone, J. M., R. R. Meier, O. A. Kelley, R. J. Thomas, K. F. Dymond, and R. P. McCoy, Investigation of ionospheric O^+ remote sensing using the 834 Å airglow, *J. Geophys. Res.*, *102*, 2441, 1997b.

Press, W. H., S. A. Teukolsky, W. T. Vetterling, and B. P. Flannery, *Numerical Recipes*, 2nd ed., Cambridge Univ. Press, New York, 1992.

Reynolds, M. A., G. Ganguli, J. A. Fedder, and D. J. Melendez-Alvira, Effect of diurnal convection on trapped thermal plasma in the outer plasmasphere, *Geophys. Res. Lett.*, *24*, 2255, 1997.

Scholer, M., D. Hovestadt, and G. Morfill, Energetic He^+ ions from the radiation belt at low altitudes near the geomagnetic equator, *J. Geophys. Res.*, *80*, 80, 1975.

Tarantola, A., *Inverse Problem Theory*, Elsevier, New York, 1987.

Tarantola, A., and B. Valette, Generalized nonlinear inverse problems solved using the least squares criterion, *Rev. Geophys.*, *20*, 219, 1982.

Weiss, L. A., R. L. Lambour, R. C. Elphic, and M. F. Thomsen, Study of plasmaspheric evolution using geosynchronous observations and global modeling, *Geophys. Res. Lett.*, *24*, 599, 1997.

Weller, C. S., and R. R. Meier, First satellite observations of the He^+ 304 A radiation and its interpretation, *J. Geophys. Res.*, *79*, 1572, 1974.

Williams, D. J., E. C. Roelof, and D. G. Mitchell, Global magnetospheric imaging, *Rev. Geophys.*, *30*, 183, 1992.

Yoshikawa, I., M. Nakamura, M. Hirahara, Y. Takizawa, K. Yamashita, H. Kunieda, T. Yamazaki, K. Misaki, and A. Yamaguchi, Observations of He II emission from the plasmasphere by a newly developed EUV telescope on board sounding rocket S-520-19, *J. Geophys. Res.*, *102*, 19897, 1997.

G.I. Ganguli and M.A. Reynolds, Plasma Physics Division, Naval Research Laboratory, Code 6794, Washington, D. C., 20375. (gang@ppd.nrl.navy.mil; anthony@ppdu.nrl.navy.mil)

A.C. Nicholas, E.O. Hulburt Center for Space Research, Naval Research Laboratory, Code 7623, Washington, D. C., 20375. (nicholas@uap.nrl.navy.mil)

R.R. Meier, D.J. Melendez-Alvira, and J.M. Picone, E.O. Hulburt Center for Space Research, Naval Research Laboratory, Code 7640, Washington, D. C., 20375. (meier@uap.nrl.navy.mil; melendez@uap.nrl.navy.mil; picone@uap.nrl.navy.mil)

E.C. Roelof, Applied Physics Laboratory, Johns Hopkins University, Laurel, MD 20723. (Edmond_Roelof@jhuapl.edu)

(Received January 27, 1998; revised March 26, 1998; accepted March 30, 1998.)